High mechanical properties and microwave absorption performances of SiCw/Si$_3$N$_4$ ceramic composites

Jie Jing[1,2], Yujun Zhao[3], Adil Saleam[1,4], Hongyu Gong[1,2,*] (ID), Yujun Zhang[1,2,*], Mingming Sheng[1,2], and Junbin Lu[1,2]

[1] Key Laboratory for Liquid-Solid Structural Evolution & Processing of Materials of Ministry of Education, Shandong University, Jinan 250061, People's Republic of China

[2] Key Laboratory of Special Functional Aggregated Materials, Ministry of Education, Shandong University, Jinan 250061, People's Republic of China

[3] School of Materials Science and Engineering, Qilu University of Technology (Shandong Academy of Sciences), Jinan 250353, China

[4] College of Mechatronics and Control Engineering, College of Physics and Optoelectronic Engineering, Shenzhen University, Shenzhen 518060, People's Republic of China

ABSTRACT

In this work, a structural–functional integrated SiCw/Si$_3$N$_4$ composite with high mechanical and microwave (MW) absorption properties was prepared by hot pressing at 1800 °C. By adding the amount of 20 wt% SiC whiskers (SiCw), the SiCw/Si$_3$N$_4$ composite achieved excellent relative density (98.6%) and mechanical properties, i.e., bending strength (938.6 ± 40.7 MPa), fracture toughness (9.40 ± 0.72 MPa m$^{1/2}$), hardness (20.5 ± 0.8 GPa) and Young's modulus (216.3 ± 21.7 GPa). Additionally, the SiCw/Si$_3$N$_4$ composite exhibits an effective absorption bandwidth of 2.74 GHz at 1.6 mm thickness. The improved mechanical properties were mainly attributed to crack deflection and pullout of SiCw and Si$_3$N$_4$ grains. Meanwhile, the improved MW absorbing properties of the material were due to the dielectric loss of the SiC phase and good impedance matching. Overall, the SiCw/Si$_3$N$_4$ composite presented in this study demonstrates the potential for the preparation of structural and functional integrated ceramics.

1 Introduction

With the development of science and technology, the structures and components of various devices are emerging towards integration, miniaturization, and multi-fictionalization, providing a novel and promising direction for the structural–functional composite materials [1–4]. Recently, to meet the advanced requirements in the military and aerospace industries, ceramic-based high-temperature microwave (MW) absorbing materials have been investigated to achieve excellent mechanical properties, oxidation resistance, creep resistance, high-

Address correspondence to E-mail: hygong@email.sdu.edu.cn; yujunzhangcn@sdu.edu.cn

temperature resistance, as well as high efficiency of MW absorption [5–7].

Based on the electromagnetic wave (EMW) propagation laws, MW absorbing composites are typically designed to contain MW absorbers and a low dielectric constant matrix. The MW absorbers can attenuate MW energy through magnetic loss, conductive loss, and dielectric loss, mainly involving ferromagnetic particles (Fe, Cu, Ni, and ferrites, etc.), carbon materials (carbon black, graphite, carbon nanotubes, and short-cut carbon fibers, etc.), and dielectric phases (SiC, TiO_2, and ZnO, etc.) [8–13]. Metal-based absorbers and polymer matrices are not suitable for applicating at high temperatures and harsh environments, due to their limitations of low oxidation temperature and Curie temperature. Therefore, ceramic composites have been considered the most promising candidates as high-temperature MW absorbing materials, such as C/C composites, SiC/Si_3N_4 composites, SiC/Al_2O_3 composites, etc. [14–17].

Si_3N_4 has a lower dielectric constant and better dielectric insulating properties, making it an ideal matrix for high-temperature MW absorbing materials [18–22]. In addition, Si_3N_4 exhibits excellent mechanical properties, high-temperature, and thermal shock resistance, thereby providing optimal attributes for composites [23–29]. As a dielectric loss MW absorber, SiC has a broad MW absorption frequency range, outstanding high-temperature mechanical properties, low density, and excellent thermal and chemical stability. Consequently, numerous combinations of Si_3N_4 and SiC ceramics have been reported for MW absorption [30–35]. Zheng et al. [30] investigated the MW absorbing properties of SiC/Si_3N_4 composite ceramics fabricated by chemical vapor infiltration (CVI), revealing the minimum reflection loss (RL) of − 27.1 dB and effective absorption bandwidth (EAB) of 2.80 GHz. Yin et al. [36] fabricated SiC/Si_3N_4 ceramics with a minimum RL of − 22.35 dB and EAB of 1.09 GHz by combining gel-casting and carbothermal reduction. However, so far, the study of SiC/Si_3N_4 MW absorbing ceramics has been hindered by factors such as impedance matching. As a result, most research has focused on using porous Si_3N_4 as the matrix, which has inferior mechanical properties and cannot be utilized in load-bearing environments. Some critical fields, such as military, medical, aerospace, etc.,

require a combination of stealth and high-temperature mechanical properties [37–39].

In this work, a novel structurally and functionally integrated $SiCw/Si_3N_4$ composite was fabricated, which exhibited high mechanical and wave-absorbing properties, using SiC whisker as a synergistic MW absorber and strengthened phase, and Si_3N_4 as matrix via vacuum hot-press sintering. SiCw, due to the low dimensionality and shape effects, not only exhibited a good MW absorbing property, but also played the role of a mechanical reinforced phase [40–44]. The influence of SiCw content on the microscopic morphology of Si_3N_4 ceramics, as well as mechanical, and MW absorbing properties was studied in detail.

2 Experimental

Commercially available α-Si_3N_4 (∼ 0.5 μm of particle size, purity > 93%, Beijing Ziguang Co Ltd., China) and SiCw (∼ 0.1 μm of diameter, ∼ 5–10 μm of length, purity > 99%, ENO Material Co Ltd., China) were used as raw materials. Magnesium oxide and yttrium oxide (Shanghai Macklin Biochemical Technology Co. Ltd., China) were added as sintering additives. A list of raw material compositions to prepare $SiCw/Si_3N_4$ composites is depicted in Table 1. To improve the nitridation rate and sintering activity, raw materials were ball-milled in a planetary ball mill machine with ethanol and homogenized at 3000 rpm for 25 min using zirconia balls. The as-prepared powder mixtures were dried and sieved with a filter (mesh size of 150 μm). Subsequently, the mixed powders were transferred into a graphite mold having an inner diameter of 42 mm, followed by hot-press sintering at 1800 °C under a vacuum with a uniaxial pressure of 30 MPa and kept for 1 h (heating rate was 5 °C/min).

Archimedes' method was employed to measure the bulk density of the disk-like composite samples. The phase compositions of the composites were identified by X-ray diffractometer (XRD, D/MAX-Ultima IV, Rigaku, Japan, λ = 1.5418 Å). The hardness and Young's modulus of the composites were analyzed by tribo-Indenter (Hysitron TI980, Bruker, America). The microstructural properties were performed by field emission scanning electron microscope (FESEM, JSM-7800F, JEOL, Japan) and transmission electron microscopy of cold field

Table 1 Compositions of the SiCw/Si$_3$N$_4$ composites

Composite label	Compositions (wt%)			
	Si$_3$N$_4$	SiCw	MgO	Y$_2$O$_3$
SC00	100	0	2.05	2.95
SC01	99	1	2.05	2.95
SC02	98	2	2.05	2.95
SC03	97	3	2.05	2.95
SC04	96	4	2.05	2.95
SC05	95	5	2.05	2.95
SC10	90	10	2.05	2.95
SC20	80	20	2.05	2.95

emission (TEM, JEM-F200, JEOL, Japan). The dielectric and MW absorption parameters were obtained by a vector analyzer (Agilent Technologies, N5222A) in the frequency range of 8.2–12.4 GHz (X-band). The size of specimens for the MW dielectric and MW absorption parameters test was 22.88 × 10.16 × 4 mm^3. The electrical conductivities were determined via the standard circular three-electrode method using the super high resistance tester (ST2643, JingGe Electronics, China).

3 Result and discussion

3.1 Characterization

Figure 1a shows the XRD patterns of raw materials (Si$_3$N$_4$ and SiCw) and SiCw/Si$_3$N$_4$ ceramic composites with different SiCw contents (0, 1, 2, 3, 4, 5,10 and 20 wt%). It can be observed that there are only β-Si$_3$N$_4$ and SiC existing in the composites after sintering. All α-Si$_3$N$_4$ phase of raw material transformed to β-phase after hot-press sintering at 1800 °C. Furthermore, the peak intensities for β-Si$_3$N$_4$ of composites remain almost constant with the increasing content of SiCw, showing that the addition of SiCw does not affect the phase transformation of Si$_3$N$_4$. As the content of SiCw increases, the peak of SiC gradually rises. But when the content reaches 20wt%, the peak of SiO$_2$ appears, which means the addition of large amounts of SiCw introduces a large number of defects in the sample, leading to a susceptibility to oxidation.

3.2 Density and mechanical properties of SiC$_w$/Si$_3$N$_4$ composite

Figure 1b shows the densities of SiCw/Si$_3$N$_4$ composites. With the increase of SiCw content, the density and relative density of ceramics increase from 3.16 g/cm^3 and 97.2% for SC00 to 3.19 g/cm^3 and 98.1% for SC03, then decrease slightly to 3.17 g/cm^3 and 97.5% for SC05, respectively. With the progressive incorporation of SiCw, the density and relative density of the composite material were observed to rise to 3.22 g/cm^3 and 98.9% for SC10, respectively, before subsequently decreasing to 3.20 g/cm^3 and 98.6% for SC20.

The fracture toughness and flexural strength of SiCw/Si$_3$N$_4$ composites with different SiCw contents are presented in Fig. 1c. It can be observed that the fracture toughness increases significantly (6.82 to 10.06 MPa m$^{1/2}$) with the SiCw adding. The superior fracture toughness (11.9 MPa m$^{1/2}$) is obtained when the content of SiCw reaches 3 wt%. With the increase of SiCw addition, the bending strength of ceramics also increases from 916.5 to 1011.5 MPa for SC00 and SC05, respectively. However, upon further addition of SiCw, the bending strength of the composite gradually decreases, while the fracture toughness begins to increase. Eventually, the bending strength and fracture toughness for SC20 are 938.66 MPa and 9.40 MPa·m$^{1/2}$, respectively. Figure 1d shows the values of hardness and Young's modulus measured by nanoindentation for all the composites. The hardness decreases from 25.2 to 21.9 GPa, and Young's modulus falls from 233.9 to 208.5 GPa, respectively, with the addition of SiCw from 0 to 2 wt%. As the SiCw content increased, the hardness and Young's modulus initially increased and then decreased upon further addition of SiCw. The values of hardness and Young's modulus of SC10 samples, which exhibit the optimal performance, are 24.75 and 217.15 GPa, respectively.

3.3 Dielectric properties of SiC$_w$/Si$_3$N$_4$ composite

The X-band (8.2–12.4 GHz) is a critical radar band for detecting high-speed aircraft. Figure 2a and b show the behavior of real and imaginary parts of the permittivity in the X-band for all composites. The relative complex permittivity ($\varepsilon_r = \varepsilon' - j\varepsilon''$) is a primary parameter that characterizes the dielectric or
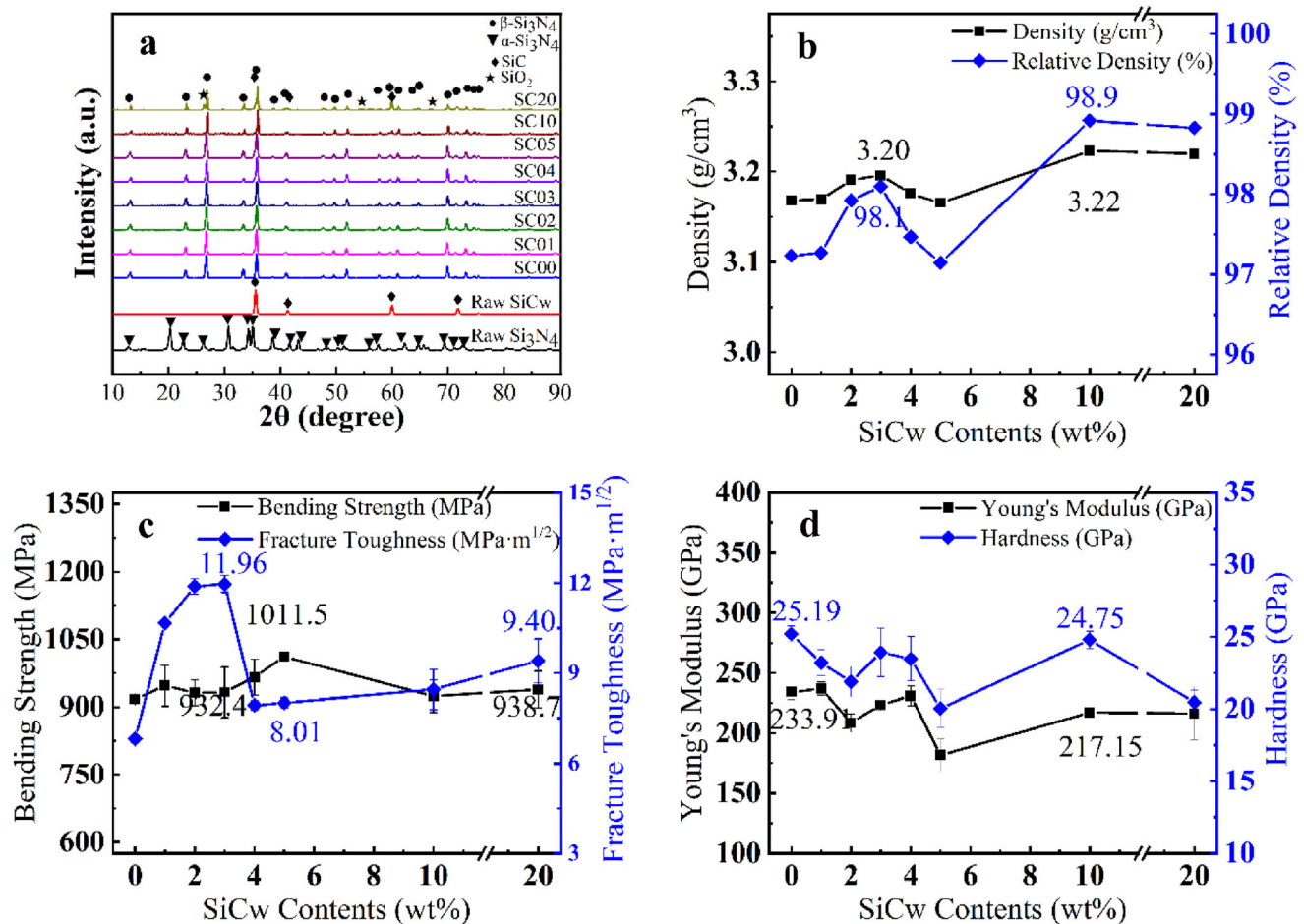
Fig. 1 XRD patterns (**a**), bulk density and relative density (**b**), bending strength and fracture toughness (**c**), and Young's modulus and hardness (**d**) of SiCw/Si$_3$N$_4$ composites

polarization of the material. The real (ε') and imaginary (ε'') parts of the permittivity represent the ability to store and dissipate electrical energy, respectively. The result indicates that the real and imaginary parts of the permittivity of Si$_3$N$_4$ ceramic, without the SiCw, are 6.99–7.49 and 0.002–0.024, respectively. The ε' and ε'' increase with the increasing SiCw content at the whole X-band. As the SiCw filling amount reaches to 5wt%, the ε' and ε'' go up to 26.8–30.60 and 1.92–4.72, respectively. As the SiCw content further increases, the ε' decreases while the ε'' continues to increase. Eventually, when the SiCw content reaches 20wt%, ε' and ε'' are 17.04–20.97 and 8.21–9.20, respectively. According to Debye's theory, a strong interfacial interaction between grain boundaries can lead to strong polarization effects. Therefore, the increase in the real and imaginary part of the permittivity can be attributed to the presence of SiCw. The dielectric loss ($\tan\sigma_\varepsilon = \varepsilon''/\varepsilon'$) can be observed in Fig. 2c. The dielectric loss tangents signify the MW attenuation property of composites. The results show that with the increase of SiCw content, the loss tangent also increases, from 0.012–0.033 to 0.391–0.544. The attenuation constant (α) is the parameter that indicates the attenuation of MW during transmission, the values of α could be obtained by Eq. (1) [45],

$$\alpha = \frac{\sqrt{2}\pi f}{c} \times \sqrt{-\varepsilon' + \sqrt{(\varepsilon')^2 + (\varepsilon'')^2}} \qquad (1)$$

Figure 2d shows the α curves of composites with different SiCw content. By Fig. 2d, the α values become higher with the addition of SiCw. Among them, the α_{max} of SC05 composite reaches above 230 at high frequency.

The MW absorption properties of the composites are characterized by the reflection loss (RL), based on the transmission line theory, using the Eqs. (2) and (3) [46],
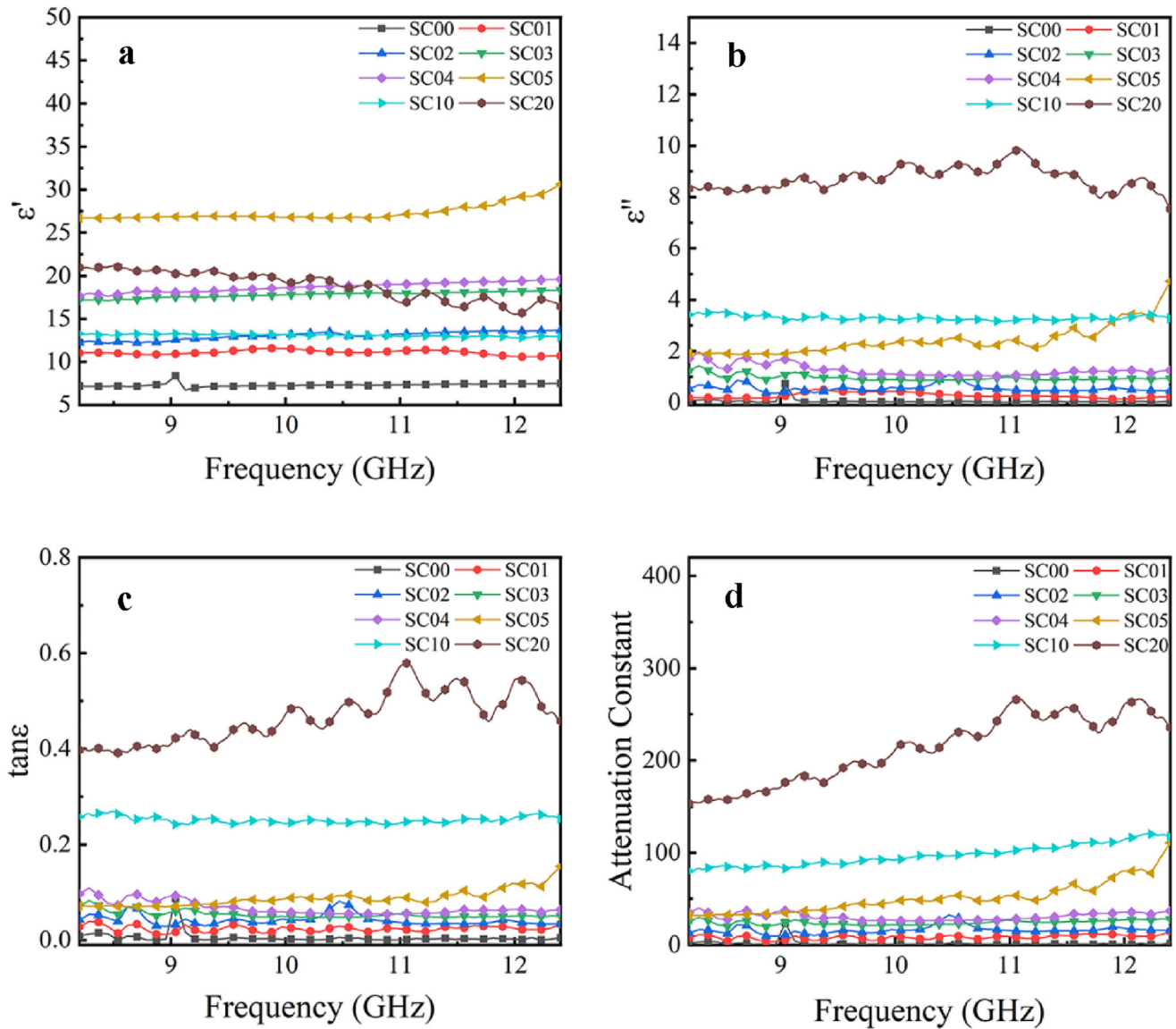
Fig. 2 Frequency dependence on the real part of permittivity (**a**), the imaginary part of permittivity (**b**), dielectric loss (**c**), and Attenuation Constant (**d**) of SiCw/Si$_3$N$_4$ composites

$$RL = 20\lg\left|\frac{Z_{in} - 1}{Z_{in} + 1}\right| \tag{2}$$

$$Z_{in} = \sqrt{\frac{\mu_r}{\varepsilon_r}}\tanh\left[j\left(\frac{2f\pi d}{c}\right)\sqrt{\mu_r\varepsilon_r}\right] \tag{3}$$

where the Z_{in} refers to the input impedance, obtained by Eq. (3) with the real and imaginary parts of the permittivity. The RL values of each sample at different thicknesses have been calculated, and the 3D images of RL are shown in Fig. 3. The value of RL less than -10 dB indicates that more than 90% of the MW could be absorbed by the materials. For Si$_3$N$_4$ composites without SiCw addition, there is an

absorption peak of minimum reflection loss (RL$_{min}$) of -10.93 dB with a thickness of 8.6 mm, which could be due to the resonance peak at the position of 9.04 GHz for Si$_3$N$_4$ ceramic matrix. The RL$_{min}$ of -23.43 dB with the adequate EAB of 0.49 GHz at the thickness of 9.9 mm at 10.39 GHz frequency is achieved with the 2 wt% of SiCw content. The RL$_{min}$ of -44.96 dB value for SiCw/Si$_3$N$_4$ composites with 3 wt% of SiCw is achieved at 9.04 GHz frequency with an EAB of 0.32 GHz and the thickness of 9.9 mm. The RL$_{min}$ reached up to -44.19 dB with an EAB of 0.42 GHz at a thickness of 8.9 mm at 9.84 GHz frequency with 4 wt% of SiCw. The RL$_{min}$
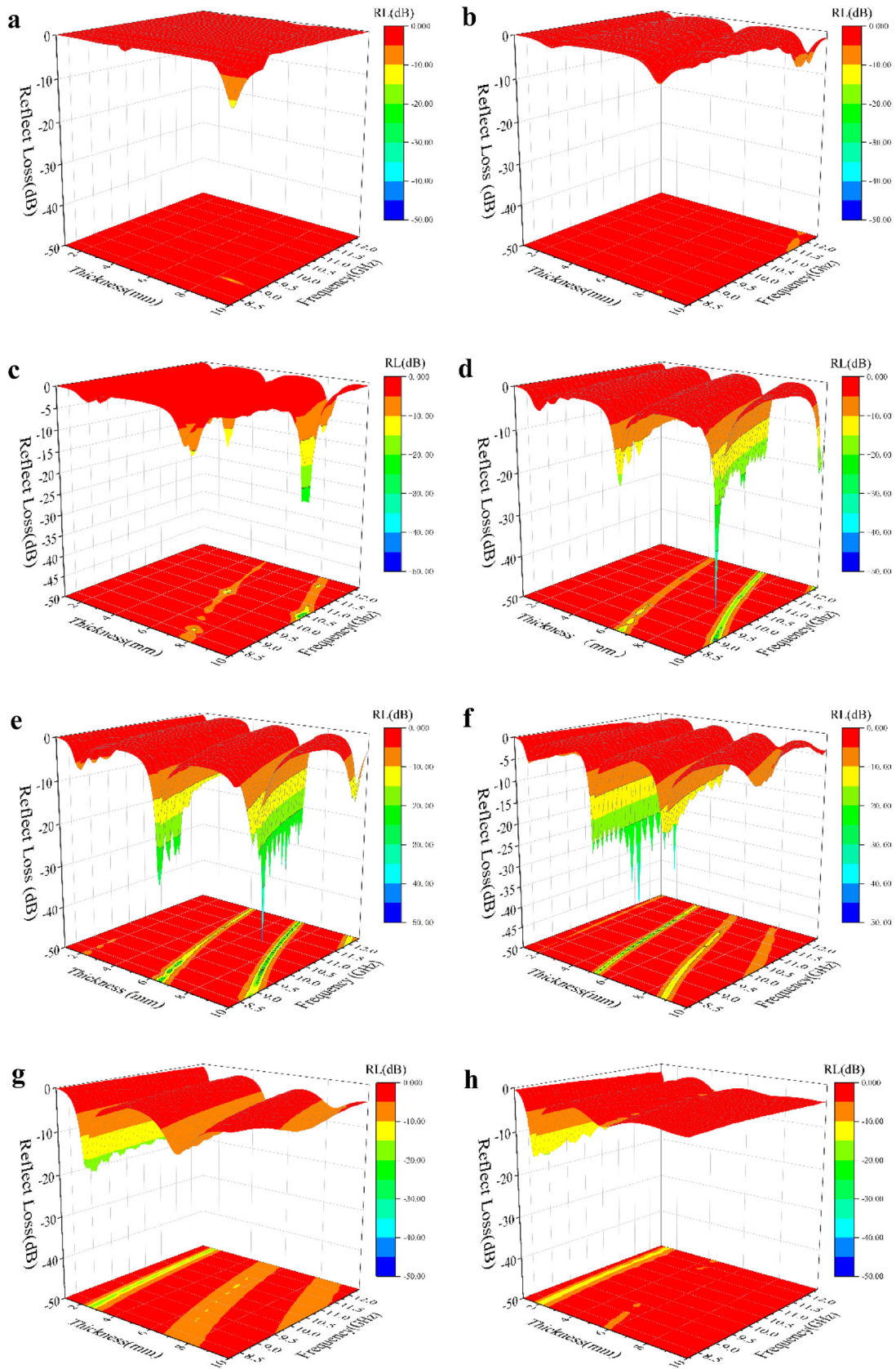
◄**Fig. 3** Three-dimensional patterns of reflection loss of the SiCw/ Si₃N₄ ceramics composites versus frequency and thickness of SC00 (**a**), SC01 (**b**), SC02 (**c**), SC03 (**d**), SC04 (**e**), SC05 (**f**), SC10 (**g**), and SC20 (**h**)

for SiCw/Si₃N₄ composites with 5 wt% of SiCw is achieved − 42.11 dB at 9.88 GHz frequency with a material thickness of 4.4 mm, and the EAB is 0.58 GHz. At a SiCw content of 10wt%, the sample exhibits RL_{min} of 17.2 dB and an EAB of 2.13 GHz when the frequency is 11.5 GHz and the thickness is 1.9 mm. when the Content of SiCw reaches 20 wt%, RL_{min} of SiCw/Si₃N₄ composites achieves a value of 16.23 dB at the 8.57 GHz and the thickness of 1.6 mm. The above results indicate that the addition of SiCw could effectively improve the MW absorbing performance of composites.

3.4 The mechanisms of the toughening and MW absorption

Figures 4 and 5 show the SEM images of the fracture surface and the polished surface of the SiCw/Si₃N₄ composites. It can be observed that SiCw/Si₃N₄ composites are dense with few pores, which is consistent with Fig. 1b. The Si₃N₄ grains exhibit a long rod-shaped morphology, which is typical of the β-phase, and the result is consistent with the XRD. Furthermore, the SiCw is uniformly distributed at the Si₃N₄ grain boundaries, and some SiCw overlaps in the matrix due to higher SiCw contents. According to Fig. 5, the aspect ratios (G_{AR}) and average grain sizes (G_{Avg}) of the Si₃N₄ have been measured (Table 2), to analyze the effect of SiCw on the matrix. With the increase of SiCw content, the G_{AR} of the composites rises first and then decreases, and the maximum value of 6.76 ± 2.20 appears with the 3 wt% SiCw contents. It indicates that with the addition of SiCw, the axial growth rate of rod grains is higher than radial and promotes the longer rod grain growth and with the excessive content of SiCw, its axial growth rate decreases. In turn, G_{Avg} showed a trend of first decreasing and then increasing. The G_{Avg} declines from 0.307 to 0.266 μm for SC00 and SC03, respectively. Therefore, the composite with 3 wt% SiCw has a smaller particle size and a larger aspect ratio, which contributes to the improvement of bending strength and fracture toughness of the composite.

After being mixed by ball milling, SiCw is randomly dispersed in the ceramic matrix. During the liquid-phase sintering, the α phase of Si₃N₄ dissolves and the β phase precipitates, while the grains adjacent to SiCw tend to grow up along the whisker's direction, and then the whiskers are wrapped between the Si₃N₄ rod-like grains, by the effect of dissolution–precipitation and liquid-phase viscous flow [6]. The growth direction of β-Si₃N₄ is influenced by the various distribution directions of SiCw, which limits the growth of β-Si₃N₄ and acts to refine the grains, as shown in Fig. 4b–d, where SiCw is circled in red. However, the excessive SiCw could form a rigid network due to the bridging and agglomeration of whiskers, as shown in Fig. 4f. which inhibit the shrinkage and densification of the SiCw/Si₃N₄ composites during sintering by forming some defects, such as large holes, and improving the resistance to mass transportation during particle rearrangement higher SiCw contents [47]. Thus, with the increase of the SiCw content, the density of the composites increased and then decreased with the further addition of SiCw. With the gradual increase in SiCw content, the ceramic tends to develop more internal defects, resulting in the formation of SiO₂ within the matrix (as depicted in Fig. 1a). This SiO₂ component fills the holes around the clustered SiCw, thus counteracting the negative impact of whisker aggregation on the material's density and leading to an overall enhancement in its density, as shown in Fig. 1b.

In addition, the analysis presented in Fig. 4 inhibits that fracture behaviors of composites primarily involves trans-granular fracture, with grains pull-out being also observed. By the Vickers hardness crack propagation path of SC03 composite, as shown in Fig. 6, it can be observed that apart from the SiCw pull-out (Fig. 6d), the self-toughening effect of rod-like β-Si₃N₄ is similar to whisker toughening, including pulling out (Fig. 6b), crack bridging (Fig. 6a) and crack deflection (Fig. 6c) of Si₃N₄ grain. During the fracture process of ceramics, the propagation of cracks in the ceramic matrix requires a significant amount of fracture energy, which can improve the toughness of ceramics. Wang et al. [48] investigated the effects of the orientation of SiCw on SiCw/Si₃N₄ composites, indicating that whisker bridging, whisker pull-out, and matrix damage are the essential toughening mechanisms for whiskers. Therefore, for SiCw/Si₃N₄ composites of this work,
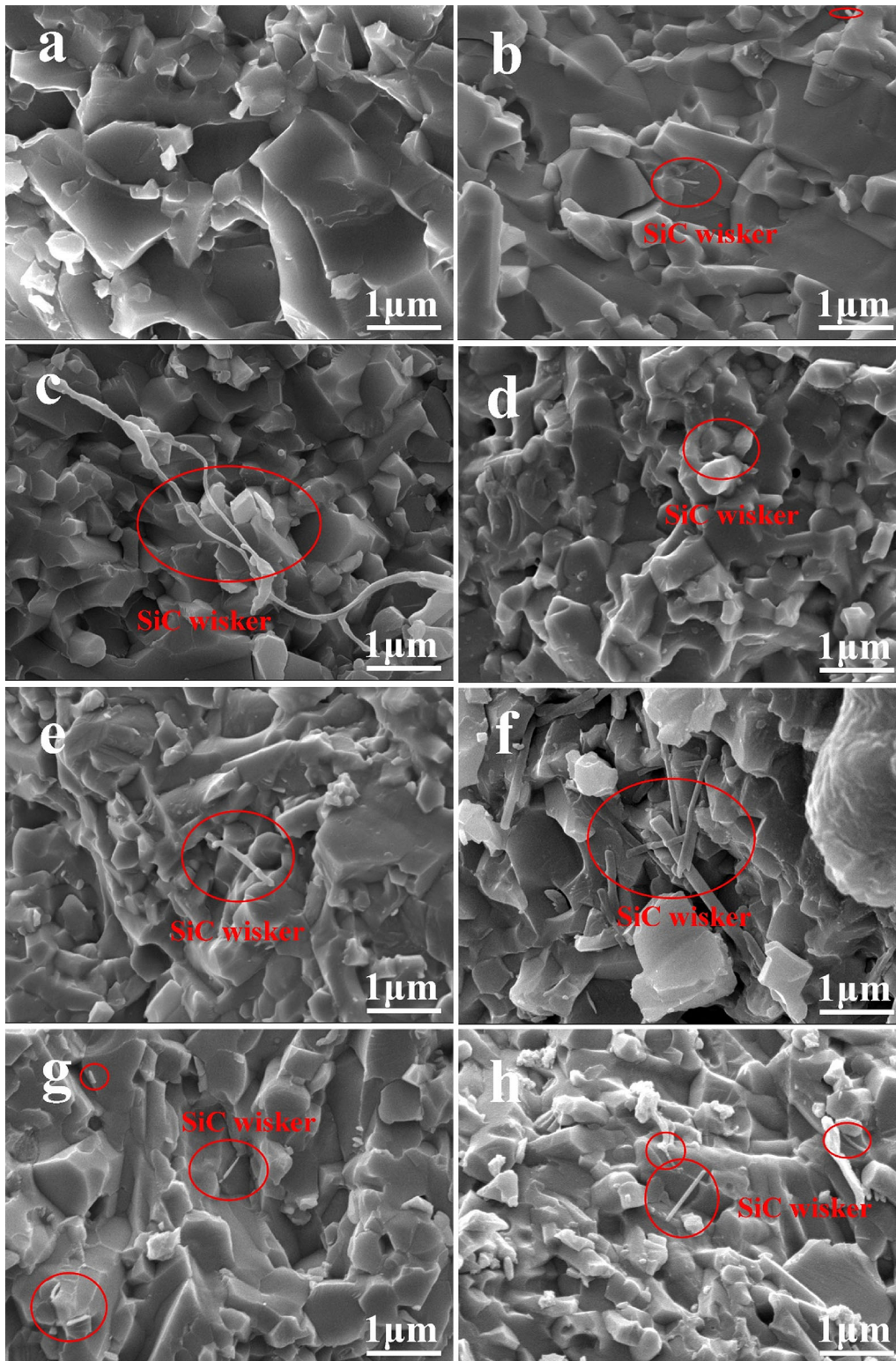
Fig. 4 SEM images of the fracture surface of SC00 (**a**), SC01 (**b**), SC02 (**c**), SC03 (**d**), SC04 (**e**), SC05 (**f**), SC10 (**g**), and SC20 (**h**)
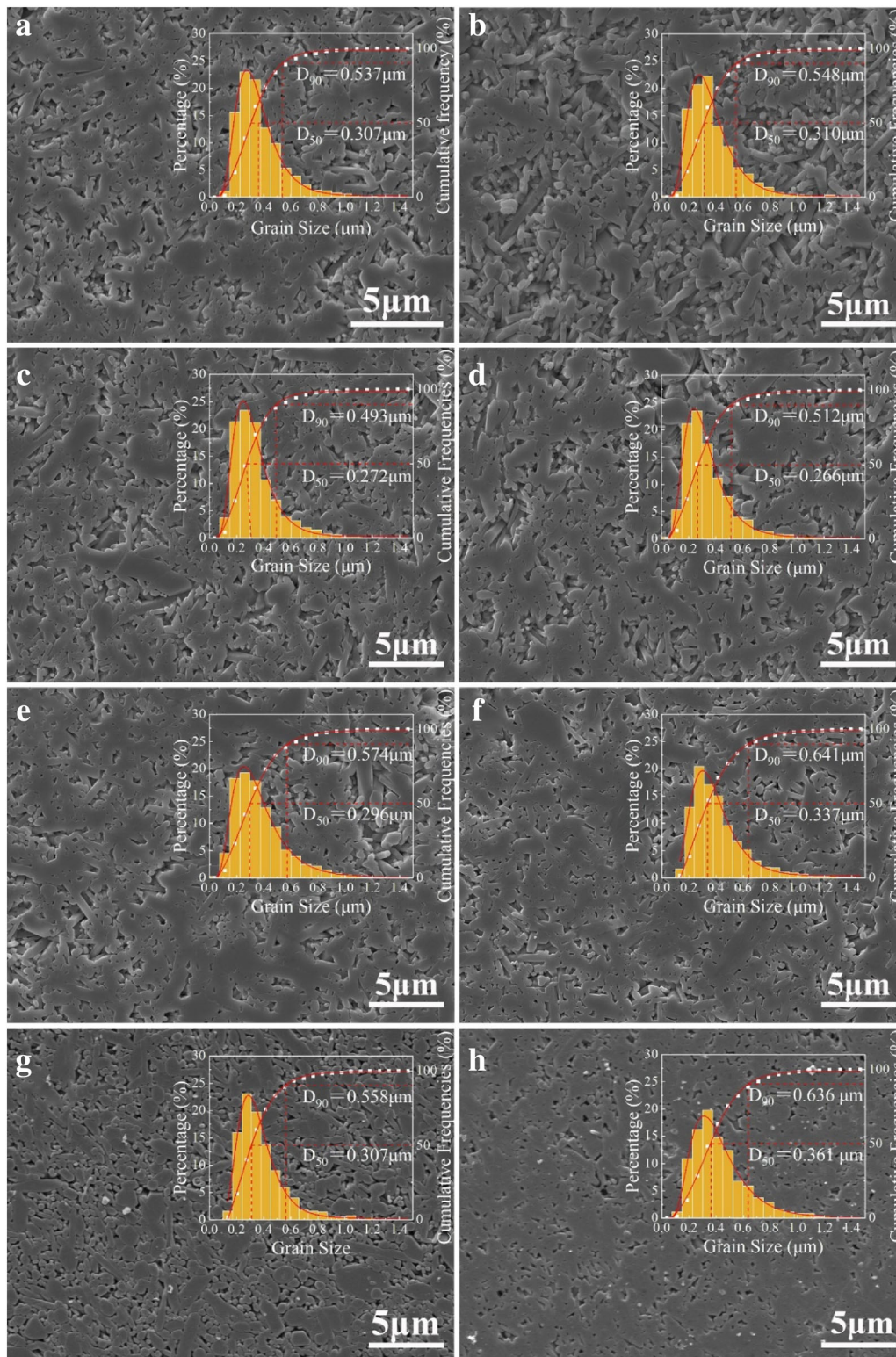
Fig. 5 SEM images of the polished surface and the grain size distribution of SC00 (**a**), SC01 (**b**), SC02 (**c**), SC03 (**d**), SC04 (**e**), SC05 (**f**), SC10 (**g**), and SC20 (**h**)

Table 2 Grains dimension of the SiCw/Si$_3$N$_4$ composites

Composite label	Grains dimension	
	Aspect ratio	Average grain sizes (μm)
SC00	6.15 ± 1.84	0.307
SC01	6.27 ± 2.00	0.310
SC02	6.76 ± 2.20	0.272
SC03	6.74 ± 1.66	0.266
SC04	6.56 ± 1.73	0.296
SC05	6.17 ± 1.99	0.337
SC10	5.51 ± 1.42	0.307
SC20	4.90 ± 1.18	0.361

self-toughening effect of the rod-like β-Si$_3$N$_4$ and the whisker-toughening effect of SiCw.

TEM images are performed for the SC03 sample. Figure 7a shows the interface between Si$_3$N$_4$ and SiCw. Figure 7b displays the TEM image of the interface between Si$_3$N$_4$ grains, revealing a continuously coherent structure without a glass phase. Combined with selected area electron diffraction (SEAD) patterns, the interplanar spacing under the Si$_3$N$_4$ grain is 0.316 nm, and the direction extends to the (200) crystal plane. The interplanar spacing of the upper crystal grain is 0.230 nm, and the direction is along the (111) crystal plane.
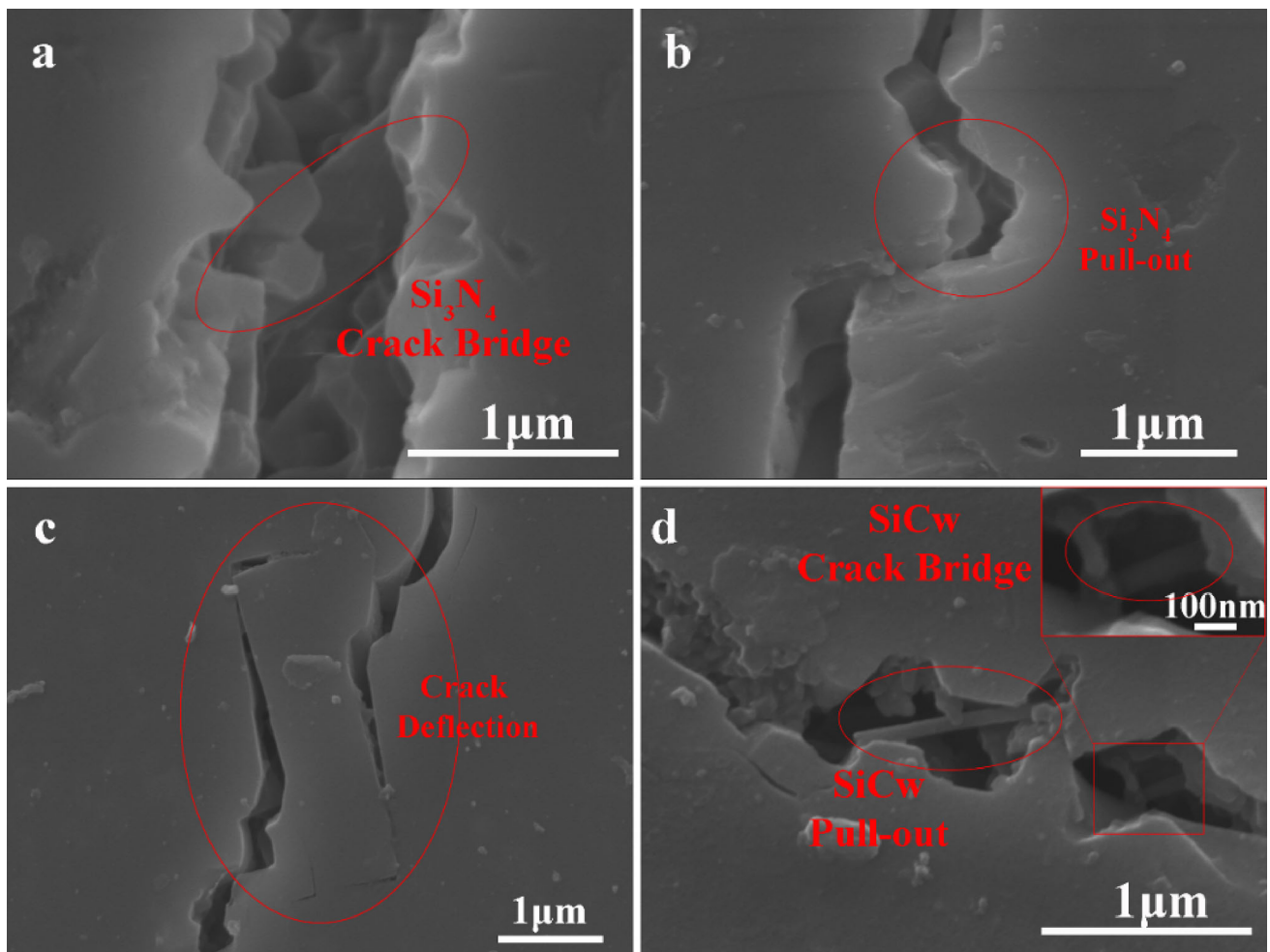

Fig. 6 SEM images of Vickers indentation fractured surfaces of SC03 sample indicate the toughening mechanisms: Si$_3$N$_4$ pull-out (**a**), Si$_3$N$_4$ crack bridge (**b**), Crack deflection (**c**), SiCw pull-out and crack bridge (**d**)

the excellent mechanical properties of the SiCw/Si$_3$N$_4$ composites can be attributed mainly to both the

The α-Si$_3$N$_4$ as the raw material for this work is entirely transformed into β-phase by the sintering aid during sintering at high temperature. At the same
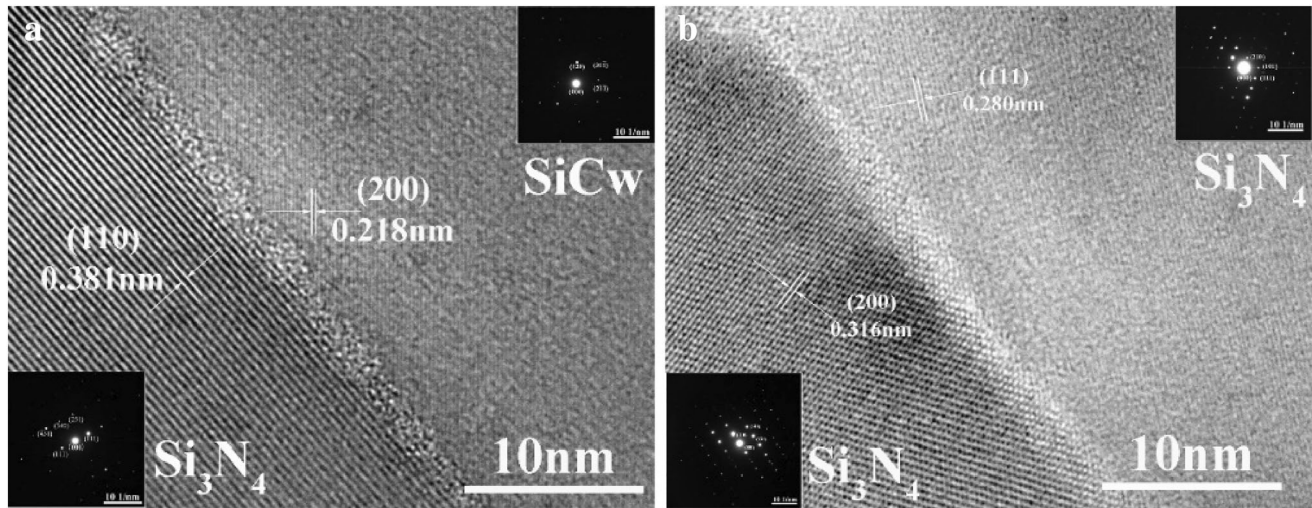
Fig. 7 TEM images and SAED patterns of the interfaces between the Si_3N_4 and SiCw of SC03 (**a**), TEM images and SAED patterns of the interfaces between the Si_3N_4 (**b**)

time, the sintering aids transforming into the liquid phase, which fills the pores between the grains, promotes the exclusion of pores, and makes the grains bond tightly. Furthermore, the addition of SiCw changes the morphology of the Si_3N_4. Due to a higher coefficient of thermal expansion of SiCw, the shrinkage of the whiskers is higher than that of the matrix during cooling, weakening the interfacial bonds between SiCw and Si_3N_4. According to a study by Wang et al. [48], when the whisker directions become similar and there is weak interfacial bonding between the matrix and the whisker, the fracture toughness in this direction significantly increases. The addition of SiCw inhibits the abnormal growth of Si_3N_4 grains, which results in a more homogeneous gain size with a certain aspect ratio. The coherent interface (Fig. 7b) between Si_3N_4 grains indicates that there is a superior interfacial bonding strength, which resists interfacial dissociation and grain pull-out. Therefore, crack extension consumes higher energy to form a new interface, which inhibits crack extension and significantly improves the toughness of the ceramics [49–53].

Figure 8 shows the relationship among RL, matching thickness (t_m) calculated by the $\lambda/4$ model, and incident impedance (Z_{in}) of SC05 composite at the entire X-band. To design the best matching thickness of absorbing materials, the quarter wavelength model (Eq. 4) is used:

$$t_m = \frac{n\lambda}{4} = \frac{nc}{4f_m\sqrt{|\mu_r||\varepsilon_r|}} \quad (n = 1, 3, 5, 7, ...) \tag{4}$$

where t_m refers to the matching thickness, λ means the wavelength of MW, and t_m represents the matching frequency. The incident EMW is completely attenuated due to the cancellation of two partially reflected waves from the interface, if the thickness of the absorbing layer equals an odd multiple of $\lambda/4$ [45, 46].

The impedance matching requires incident impedance (Z_{in}) of material matching the impedance of free space (Z_0) to reduce the reflection of electromagnet waves, which means the value of Z_{in} should be closer to 1. In general, if the Z_{in} value is between 0.8 and 1.2, it could be considered the best impedance matching range [10, 17, 54]. As shown in Fig. 8, the peaks of RL of composites with different thicknesses match the t_m curve calculated by the $\lambda/4$ model. Therefore, canceling two partially reflected waves allows composites to attenuate MW. In addition, it is obvious that the trend of RL is similar to that of the Z_{in}, as shown in Fig. 8. Moreover, the peak value of the Z_{in} curve for 3.8 mm and 4.4 mm thickness is close to 1, and the corresponding RL has the smallest reflection loss. Thus, the composite with excellent impedance matching exhibit outstanding MW absorption performance.

To analyze the relaxation mechanisms of the SiCw/Si_3N_4 composites, the ε'–ε'' curves were plotted. If the ε'–ε'' curve presents a semicircle (known as Cole–Cole circle), the loss of EMW in the interior of the composites could follow the Debye Relaxation model. Figure 9b–d show the ε'–ε'' curves of SC00,

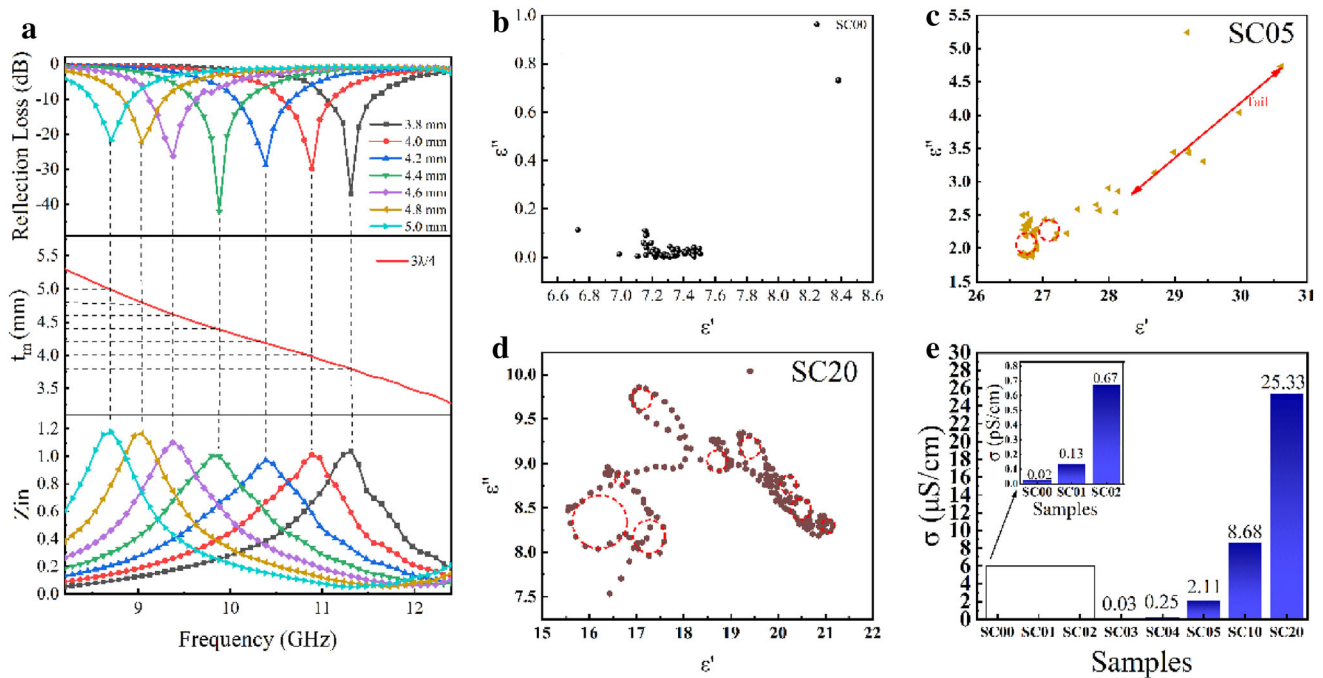**Fig. 8** Frequency dependent reflection loss, simulations of matching thickness under the λ/4 model, and corresponding impedance matching of SC05 (**a**), Cole–Cole semicircle image of SC00 (**b**), SC05 (**c**), SC20 (**d**), and Direct current Conductivity(σ) (**e**) of the SiCw/Si$_3$N$_4$ composites

SC05 and SC20. By comparing the three graphs, significant Cole–Cole circles appear in SC05, SC20 compared to SC00, indicating that the addition of SiCw provides interfacial polarization to the composites. And in contrast to SC05, SC20 exhibits a greater number of significant Cole–Cole circles, which suggests that the formation of SiO$_2$ may contribute to enhance the internal polarization losses of the ceramic material.

When the EM waves are incident inside the composites, a large number of electrons are bound to the interfacial region between SiCw and Si$_3$N$_4$ matrix, due to the difference in dielectric properties of different components, forming a spatial electric field.
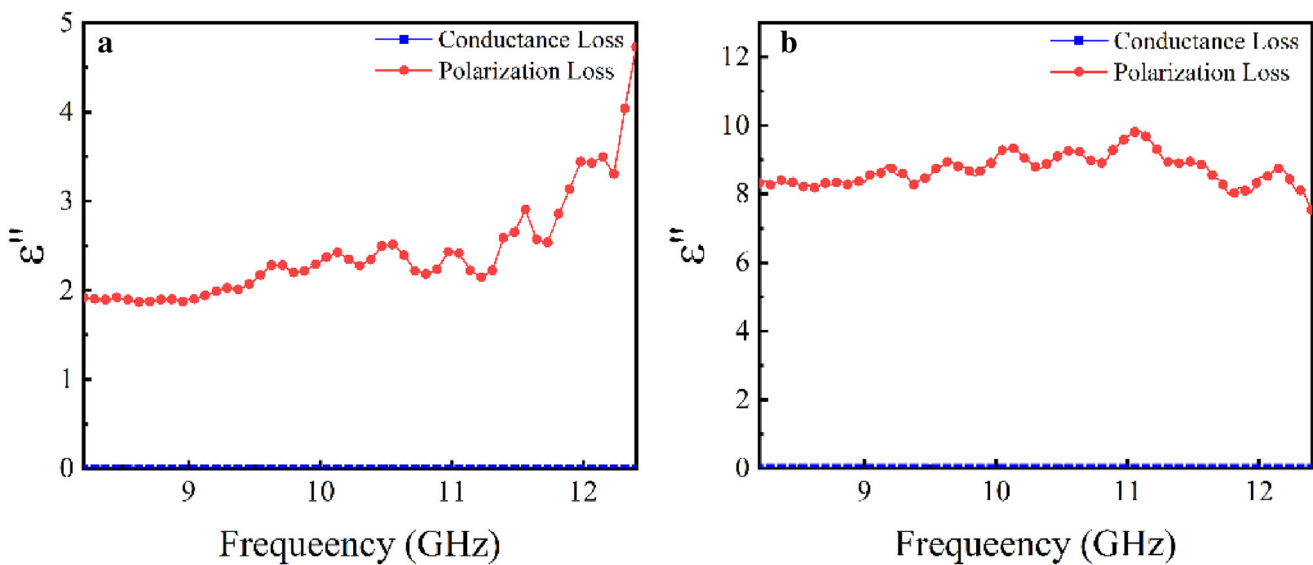

Fig. 9 The conductance loss and polarization loss values obtained by Debye equations of SC05 (**a**) and SC 20 (**b**)

Under the action of the spatial electric field, the charged center of the interface is forced to deviate from forming the interfacial polarization. In this process, the energy of the EM waves is converted to the thermal motion of the molecules[55]. The $\varepsilon'-\varepsilon''$ curves of SC05 show a 'tail' (as shown by the arrow in Fig. 9c), at a higher frequency, indicating that substantial, strong conduction losses exist in the composites. SiCw with the one-dimensional structure builds a conductive network inside the composite, providing a path for the migration of charged particles (including holes, weak electrons, etc.), promoting the rapid transport of charged particles, during which the energy of EM waves is converted into Joule heat, leading to conductivity losses [56]. In addition, a certain deviation, between the Cole–Cole circle of SC05 and the standard semicircle, indicates that besides the interface polarization, there are other mechanisms involved in the polarization loss, such as the dipole orientation relaxation loss of SiCw. As one-dimensional material, the SiCw has a large number of defects within itself, which tends to form electric dipoles that deviate from the geometric center. Under the action of the alternating EM field, the dipole moves reciprocally with the change of the electric field [42]. Due to the resistances (such as frictional resistance, etc.), a certain hysteresis occurs in the reciprocal movement of the dipole, resulting in relaxation losses [57]. In conclusion, the dielectric loss mechanism of SiCw/Si₃N₄ composites mainly consists of conductivity loss and polarization loss (including interfacial polarization and dipole relaxation loss).

By using the circular three-electrode method, the electrical conductivity (σ) of the SiCw/Si₃N₄ composites was evaluated, as depicted in Fig. 8e. According to the results, the σ of the composite increased rapidly with the increase in the content of SiCw, transitioning from a transparent material to an absorbing material, and exhibiting a rise from 2.31×10^{-8} μS/cm for SC00 to 25.33 μS/cm for SC20. Drawing from Debye theory, the dielectric loss can be expressed as the sum of the polarization loss and conductivity loss, formulated as [45]:

$$\varepsilon'' = \frac{\varepsilon_s - \varepsilon_\infty}{1 + \omega^2\tau(T)^2}\omega\tau(T) + \frac{\sigma(T)}{2\pi\varepsilon_0 f} = \varepsilon_p'' + \varepsilon_c'' \qquad (5)$$

where ε_s and ε_∞ represent the inherent frequency permittivity and the optical frequency permittivity, respectively, whereas ω signifies the angular frequency, $\tau(T)$ indicates the relaxation time, $\sigma(T)$ denotes the electrical conductivity, ε_0 stands for the dielectric constant in vacuum (8.85×10^{-12} F/m)), and f represents the frequency. Furthermore, ε_p'' and ε_c'' denote the polarization loss and conductance loss, respectively. Figure 9 presents the polarization loss and conductance loss of SC05 and SC20, computed by formula 5. As the SiCw content increases, the σ of the composite rises, resulting in a corresponding increase in the conductance loss, from 0.004 for SC05 to 0.01 for SC20. Although the conductance loss has increased significantly, the polarization loss value of 9.84 for SC20 suggests that the conductivity loss of the material is considerably lower than its polarization loss. Therefore, it can be concluded that the dielectric loss in SiCw/Si₃N₄ composites is predominantly governed by polarization loss.

Figure 10 depicts the MW absorption mechanisms of the SiCw/Si₃N₄ composites. When the MW is incident on the composite, Si₃N₄ as a matrix has a low dielectric constant and loss, which allows the maximum amount of MW to be incident inside the composite instead of reflecting. SiC has high dielectric and semi-conductivity properties. In an alternating electric field, the polarization relaxation loss, and the electrical loss of SiCw are the main factors that cause the MW absorption. The 3D conducting network formed by agglomerated SiCw could effectively extend the propagation path of dissipative MW, resulting in conductivity loss and electron polarization loss [6, 36, 58]. These mechanisms contribute to the absorption of MW in SiCw/Si₃N₄ composites.

In summary, it is apparent that the addition of SiCw as the reinforcing and absorbing phase of composites could significantly improve the MW absorption performance of the ceramics while enhancing the toughness. Table 3 presents a performance comparison of different Si₃N₄ based composite ceramics. The current research on Si₃N₄ matrix MW absorbing composites primarily used porous Si₃N₄ ceramics as the matrix with the addition of C filler and SiC filler. The ceramics have excellent MW absorbing ability, but the weak mechanical properties limit their wide application. In this paper, SiCw/Si₃N₄ composites fabricated by vacuum hot-press sintering, exhibited excellent mechanical properties and good MW absorption performance. Overall, SiCw/Si₃N₄ composites have great potential as high-performance materials for MW absorption applications.

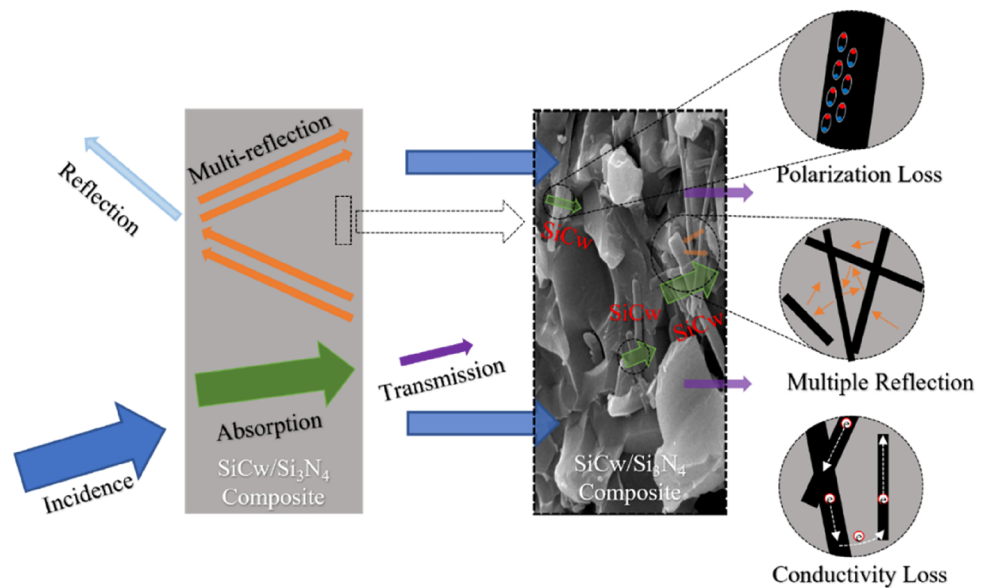**Fig. 10** Schematic diagram of microwave absorption mechanism of the $SiCw/Si_3N_4$ composites

Table 3 Comparison of mechanical performance and MW absorption performance of various Si_3N_4 composites

Matrix	Filler	RL_{min} (dB)	Thickness (mm) @RL_{min}	EAB (GHz)	Bending strength (MPa)	Fracture toughness (MPa $m^{1/2}$)	References
Si_3N_4	SiC	− 6.7	1.2	–	284	4.6	[31]
Si_3N_4	SiC_f	− 12.7	2.25	3.5	–	–	[58]
Si_3N_4	Graphene	− 26.7	3.75	4.2	–	–	[59]
Si_3N_4	RGO	− 16.7	4.3	4.2	–	–	[60]
Si_3N_4	SiC_{nw}	− 35.2	2	3.5	–	–	[61]
Si_3N_4	SiC_f	− 11.4	2.6	–	380	12.9	[34]
Si_3N_4	SiC	− 22.35	2	1.09	129.37	4.25	[36]
Si_3N_4	C_f/SiC-NFs	− 20.3 (800 °C)	2	2.3	371	7.23	[20]
Si_3N_4	SiC_{nw}	− 14.67	5.0	3.47	240.36	3.68	[17]
Si_3N_4	SiCw	− 16.23	1.6	2.74	938.66	9.40	This work

4 Conclusion

In this study, $SiCw/Si_3N_4$ composites were successfully fabricated by vacuum hot-pressing at 1800 °C. A complete phase transformation from α- to β-Si_3N_4 was achieved. Moreover, SEM and TEM results presented that SiCw was uniformly dispersed between the grain boundaries of the Si_3N_4 matrix without any impurities. A coherent structure was formed between Si_3N_4–SiCw and Si_3N_4–Si_3N_4. The addition of SiCw helped to refine the grains, increase the G_{AR} and reduce the G_{Avg} of Si_3N_4, and improve the mechanical properties of the ceramic matrix. The MW absorption performance of Si_3N_4 ceramics was also studied, the addition of SiCw as an MW absorber was found to improve the MW absorbing performance of ceramic composites.

By adding the amount of 20 wt% SiCw, the $SiCw/Si_3N_4$ composite achieved excellent relative density (98.6%) and mechanical properties, including bending strength (938.6 ± 40.7 MPa), fracture toughness (9.40 ± 0.72 MPa $m^{1/2}$), hardness (20.5 ± 0.8 GPa) and Young's modulus (216.3 ± 21.7 GPa). Additionally, the $SiCw/Si_3N_4$ composite exhibits an EAB of 2.74 GHz at 1.6 mm thickness.

Therefore, the addition of SiCw into the Si_3N_4 matrix can not only improve the mechanical properties of ceramics but also endow ceramics with certain

MW absorbing performance, which provides a new direction for the preparation of structural and functional integrated ceramics.

Author contributions

All authors contributed to the study conception and design. Material preparation, data collection and analysis were performed by JJ, YZ and JL. The first draft of the manuscript was written by JJ and all authors commented on previous versions of the manuscript. All authors read and approved the final manuscript.

Data availability

The data used to support the findings of this study are available from the corresponding author upon request.

Declarations

References

1. M. Li, X. Yin, G. Zheng, M. Chen, M. Tao, L. Cheng, L. Zhang, High-temperature dielectric and microwave absorption properties of Si_3N_4–SiC/SiO_2 composite ceramics. J. Mater. Sci. **50**, 1478–1487 (2014)

2. H. Song, W. Zhou, F. Luo, Z. Huang, Y. Qing, M. Chen, Y. Mu, Temperature dependence of dielectric properties of SiCf/PyC/SiC composites. Mater. Sci. Eng. B **195**, 12–19 (2015)

3. M.S. Charoo, M.F. Wani, Friction and wear properties of nano-Si_3N_4/nano-SiC composite under nanolubricated conditions. J. Adv. Ceram. **5**, 145–152 (2016)

4. Y. Yu, J. Li, J. Niu, F. Yi, S. Meng, The stability and repeatability of high temperature electrical properties of SiAlCN ceramic sensor heads. Ceram. Int. **45**, 7588–7593 (2019)

5. W. Duan, X. Yin, F. Cao, Y. Jia, Y. Xie, P. Greil, N. Travitzky, Absorption properties of twinned SiC nanowires reinforced Si_3N_4 composites fabricated by 3d-prining. Mater. Lett. **159**, 257–260 (2015)

6. W. Zhou, R.-M. Yin, L. Long, H. Luo, W.-D. Hu, Y.-H. Ding, Y. Li, SiC nanofibers modified Si_3N_4 ceramics for improved electromagnetic interference shielding in X-band. Ceram. Int. **44**, 2249–2254 (2018)

7. J. Niu, S. Meng, H. Jin, F. Yi, J. Li, G. Zhang, Y. Zhou, Electrical conductivity change induced by porosity within polymer-derived SiCN ceramics. J. Alloys Compds. **777**, 1010–1016 (2019)

8. X.D. Zuo, P. Xu, C.Y. Zhang, M.Z. Li, X.Y. Jiang, X.G. Yue, Porous magnetic carbon nanofibers (P-CNF/Fe) for low-frequency electromagnetic wave absorption synthesized by electrospinning. Ceram. Int. **45**, 4474–4481 (2019)

9. X. Yang, X. Lin, Y. Huang, M. Chen, Mechanical reinforced lightweight multifunctional metastructure with ultrabroadband microwave absorption. IEEE Antennas Wirel. Propag. Lett. **20**, 1023–1027 (2021)

10. X. Guo, J.B. Lu, J. Liu, C.M. Liu, Y.C. Tong, J. Li, H.B. Sun, H. Peng, S.G. Wu, Y.R. Feng, H.Y. Gong, Enhanced electromagnetic wave absorption properties of PDCs-SiCN(Ni) fibers by in-situ formed CNTs and Ni_2Si. Ceram. Int. **48**, 20495–20505 (2022)

11. N. Yang, Z.-X. Luo, S.-C. Chen, G. Wu, Y.-Z. Wang, Fe_3O_4 nanoparticle/N-doped carbon hierarchically hollow microspheres for broadband and high-performance microwave absorption at an ultralow filler loading. ACS Appl. Mater. Interfaces **12**, 18952–18963 (2020)

12. A. Saleem, Y. Zhang, H. Gong, M.K. Majeed, X. Lin, J. Jing, M. Sheng, C. Zhao, Dielectric and microwave absorption properties of fluoride-doped MWCNT/Si_3N_4 composite. J. Mater. Sci.: Mater. Electron. **31**, 2918–2925 (2020)

13. D. Dai, X. Lan, L. Wu, Z. Wang, Designed fabrication of lightweight SiC/Si_3N_4 aerogels for enhanced electromagnetic wave absorption and thermal insulation. J. Alloys Compds. **901**, 163651 (2022)

14. E. Volkmann, K. Tushtev, D. Koch, C. Wilhelmi, J. Göring, K. Rezwan, Assessment of three oxide/oxide ceramic matrix composites: mechanical performance and effects of heat treatments. Compos. A Appl. Sci. Manuf. **68**, 19–28 (2015)

15. X.Y. Yuan, L.F. Cheng, L.T. Zhang, Electromagnetic wave absorbing properties of SiC/SiO_2 composites with ordered inter-filled structure. J. Alloys Compds. **680**, 604–611 (2016)

16. G. Camus, Modelling of the mechanical behavior and damage processes of fibrous ceramic matrix composites: application to a 2-D SiC/SiC. Int. J. Solids Struct. **37**, 919–942 (2000)

17. S. Yin, Y. Jiang, K. Su, X. Fang, Y. Wang, Q. Li, J. Yang, Preparation, mechanical, dielectric and microwave absorption properties of hierarchical porous SiCnw-Si_3N_4 composite ceramics. J. Eur. Ceram. Soc. **42**, 3820–3830 (2022)

18. R. Mo, F. Ye, X. Liu, Q. Zhou, X. Fan, J. Xue, P. Zhang, L. Zhang, L. Cheng, A high-temperature structural and wave-absorbing SiC fiber reinforced Si_3N_4 matrix composites. Ceram. Int. **47**, 8191–8199 (2021)

19. H. Luo, P. Xiao, L. Huang, W. Hong, Dielectric properties of Cf–Si_3N_4 sandwich composites prepared by gelcasting. Ceram. Int. **40**, 8253–8259 (2014)

20. W. Zhou, Y. Li, L. Long, H. Luo, Y. Wang, High-temperature electromagnetic wave absorption properties of Cf/SiCNFs/Si_3N_4 composites. J. Am. Ceram. Soc. **103**, 6822–6832 (2020)

21. Z. Cai, L. Su, H. Wang, M. Niu, L. Tao, D. Lu, L. Xu, M. Li, H. Gao, Alternating multilayered Si_3N_4/SiC aerogels for broadband and high-temperature electromagnetic wave absorption up to 1000 °C. ACS Appl. Mater. Interfaces **13**, 16704–16712 (2021)

22. Q. Jiang, D. Yang, H. Yuan, R. Wang, M. Hao, W. Ren, G. Shao, H. Wang, J. Cui, J. Hu, Fabrication and properties of Si_2N_2O-Si_3N_4 ceramics via direct ink writing and low-temperature sintering. Ceram. Int. **48**, 32–41 (2022)

23. S. Chen, L. Wang, G. He, J. Li, C.-A. Wang, Microstructure and properties of porous Si_3N_4 ceramics by gelcasting-self-propagating high-temperature synthesis (SHS). J. Adv. Ceram. **11**, 172–183 (2022)

24. Z. Cheng, F. Ye, Y. Liu, T. Qiao, J. Li, H. Qin, L. Cheng, L. Zhang, Mechanical and dielectric properties of porous and wave-transparentSi_3N_4-Si_3N_4 composite ceramics fabricated by 3D printing combined with chemical vapor infiltration. J. Adv. Ceram. **8**, 399–407 (2019)

25. Y. Zhao, Y. Zhang, H. Gong, H. Sun, Q. Li, Gas pressure sintering of BN/Si_3N_4 wave-transparent material with Y_2O_3– MgO nanopowders addition. Ceram. Int. **40**, 13537–13541 (2014)

26. X. Dang, D. Zhao, T. Guo, X. Fan, J. Xue, F. Ye, Y. Liu, L. Cheng, Oxidation behaviors of carbon fiber reinforced multilayer SiC-Si_3N_4 matrix composites. J. Adv. Ceram. **11**, 354–364 (2022)

27. Y. Wang, W. Liu, J. Guo, M. Li, B. Fan, H. Wang, H. Xu, H. Lu, G. Shao, R. Zhang, L. An, In situ formation of Si_3N_4–SiC nanocomposites through polymer-derived SiAlCN ceramics and spark plasma sintering. Ceram. Int. **47**, 22049–22054 (2021)

28. Y. Fan, D. Yang, H. Mei, S. Xiao, Y. Yao, L. Cheng, L. Zhang, Tuning SiC nanowires interphase to improve the mechanical and electromagnetic wave absorption properties of SiCf/SiCnw/Si_3N_4 composites. J. Alloys Compds. **896**, 163017 (2022)

29. E. Kutlu, P. Narin, G. Atmaca, B. Sarikavak-Lisesivdin, S.B. Lisesivdin, E. Ÿzbay, Effect of substitutional As impurity on electrical and optical properties of β-Si_3N_4 structure. Mater. Res. Bull. **83**, 128–134 (2016)

30. G. Zheng, X. Yin, J. Wang, M. Guo, X. Wang, Complex permittivity and microwave absorbing property of Si_3N_4–SiC composite ceramic. J. Mater. Sci. Technol. **28**, 745–750 (2012)

31. X. Li, L. Zhang, X. Yin, L. Feng, Q. Li, Effect of chemical vapor infiltration of SiC on the mechanical and electromagnetic properties of Si_3N_4–SiC ceramic. Scr. Mater. **63**, 657–660 (2010)

32. X. Li, L. Zhang, X. Yin, Z. Yu, Mechanical and dielectric properties of porous Si_3N_4–SiC(BN) ceramic. J. Alloys Compds. **490**, L40–L43 (2010)

33. X. Liu, X. Yin, W. Duan, F. Ye, X. Li, Electromagnetic interference shielding properties of polymer derived SiC-Si_3N_4 composite ceramics. J. Mater. Sci. Technol. **35**, 2832–2839 (2019)

34. R. Mo, X. Yin, F. Ye, X. Liu, X. Ma, Q. Li, L. Zhang, L. Cheng, Electromagnetic wave absorption and mechanical properties of silicon carbide fibers reinforced silicon nitride matrix composites. J. Eur. Ceram. Soc. **39**, 743–754 (2019)

35. M. Li, L. Cheng, R. Mo, F. Ye, X. Yin, (SiC-Si_3N_4)w/SiBCN composite ceramics with tunable electromagnetic properties. J. Alloys Compds. **798**, 280–289 (2019)

36. S. Yin, D. Mao, L. Pan, X. Fang, Y. Wang, T. Qiu, J. Yang, Porous SiC–Si_3N_4 composite ceramics with excellent EMW absorption property prepared by gelcasting using DMAA. Ceram. Int. **47**, 27058–27070 (2021)

37. F. Meng, H. Wang, F. Huang, Y. Guo, Z. Wang, D. Hui, Z. Zhou, Graphene-based microwave absorbing composites: a review and prospective. Compos. B Eng. **137**, 260–277 (2018)

38. M. Zhao, Y. Liu, N. Chai, H. Qin, X. Liu, F. Ye, L. Cheng, L. Zhang, Effect of SiBCN content on the dielectric and EMW absorbing properties of SiBCN-Si_3N_4 composite ceramics. J. Eur. Ceram. Soc. **38**, 1334–1340 (2018)

39. G. Zheng, X. Yin, S. Liu, X. Liu, J. Deng, Q. Li, Improved electromagnetic absorbing properties of Si_3N_4–SiC/SiO_2 composite ceramics with multi-shell microstructure. J. Eur. Ceram. Soc. **33**, 2173–2180 (2013)

40. Y. Jiang, Y. Chen, Y.J. Liu, G.X. Sui, Lightweight spongy bone-like graphene@SiC aerogel composites for high-performance microwave absorption. Chem. Eng. J. **337**, 522–531 (2018)

41. S. Dong, Y. Lyu, X.T. Li, J.M. Chen, X.H. Zhang, J.C. Han, P. Hu, Construction of MnO nanoparticles anchored on SiC whiskers for superior electromagnetic wave absorption. J. Colloid Interface Sci. **559**, 186–196 (2020)

42. S. Dong, Y.X. Chen, C.Q. Hong, Synergetic impedance matching and loss ability towards efficient microwave absorption of Fe_3O_4 nanoparticles anchored on SiC whiskers via a simple solvothermal method. J. Alloys Compds. **838**, 155558 (2020)

43. A. Saleem, R. Iqbal, A. Hussain, M.S. Javed, M.Z. Ashfaq, M. Imran, M.M. Hussain, A.R. Akbar, S. Jun, M.K. Majeed, Recent advances and perspectives in carbon-based fillers reinforced Si_3N_4 composite for high power electronic devices. Ceram. Int. **48**, 13401–13419 (2022)

44. A. Saleem, Y. Zhang, H. Gong, M.K. Majeed, M.Z. Ashfaq, J. Jing, X. Lin, M. Sheng, Carbon nanostructure-reinforced SiCw/Si_3N_4 composite with enhanced thermal conductivity and mechanical properties. RSC Adv. **10**, 15023–15029 (2020)

45. J.B. Lu, Y.R. Feng, J. Liu, C.M. Liu, Y.C. Tong, S.G. Wu, H.B. Sun, H.Y. Gong, X. Guo, Improved electromagnetic wave absorbing performance of PDCs-SiCN(Ni) fibers with different nickel content. Ceram. Int. **48**, 23578–23589 (2022)

46. G. Logesh, U. Sabu, C. Srishilan, M. Rashad, A. Joseph, K.C. James Raju, M. Balasubramanian, Tunable microwave absorption performance of carbon fiber-reinforced reaction bonded silicon nitride composites. Ceram. Int. **47**, 22540–22549 (2021)

47. C.-A. Wang, Y. Huang, Improved sinterability of SiC(w)/Si_3N_4 composites by whisker-oriented alignment. Mater. Sci. Eng. A **390**, 319–325 (2005)

48. W. Chang-An, H. Yong, Z. Hongxiang, The effect of whisker orientation in SiC whisker-reinforced Si_3N_4 ceramic matrix composites. J. Eur. Ceram. Soc. **19**, 1903–1909 (1999)

49. F.L. Riley, Silicon nitride and related materials. J. Am. Ceram. Soc. **83**, 245–265 (2000)

50. Y. Han, S. Li, T.B. Zhu, W.W. Wu, D. An, F. Hu, F.R. Zhai, Z.P. Xie, Enhanced toughness and reliability of Si_3N_4-SiCw composites under oscillatory pressure sintering. Ceram. Int. **44**, 12169–12173 (2018)

51. T.F. Li, Y.J. Chen, W. Li, J.B. Li, L.J. Luo, T. Yang, L.Y. Liu, G.L. Wu, Fabrication and mechanical properties of boron nitride nanotube reinforced silicon nitride ceramics. Ceram. Int. **44**, 6456–6460 (2018)

52. K. Kumar, M.J. Kim, H.M. Oh, Y.J. Park, H.N. Kim, H.J. Ma, J.W. Lee, J.W. Ko, Fabrication of highly dense Si_3N_4 via record low-content additive system for low-temperature pressureless sintering. J. Am. Ceram. Soc. **105**, 4669–4680 (2022)

53. A. Saleem, Y. Zhang, H. Gong, M.K. Majeed, Fluoride doped SiC/Si_3N_4 composite as a high thermal conductive material with enhanced mechanical properties. Ceram. Int. **45**, 21004–21010 (2019)

54. Y. Feng, X. Guo, J. Lu, J. Liu, G. Wang, H. Gong, Enhanced electromagnetic wave absorption performance of SiCN(Fe) fibers by in-situ generated Fe_3Si and CNTs. Ceram. Int. **47**, 19582–19594 (2021)

55. S. Wang, H. Gong, M.Z. Ashfaq, D. Qi, X. Yue, Introducing MWCNTs conductive network in polymer-derived SiCN ceramics for broadband electromagnetic wave absorption. Ceram. Int. **48**, 23989–24002 (2022)

56. S. Wang, M.Z. Ashfaq, D. Qi, X. Yue, H. Gong, Electromagnetic wave absorption properties of polymer-derived magnetic carbon-rich SiCN-based composite ceramics. Ceram. Int. **48**, 4986–4998 (2022)

57. W. Xiao, P. Xiao, H. Luo, W. Zhou, Y. Li, Preparation and dielectric properties of Si_3N_4/SiCw composite ceramic. J. Mater. Sci.: Mater. Electron. **25**, 4088–4094 (2014)

58. Q. Li, X. Yin, L. Zhang, L. Cheng, Effects of SiC fibers on microwave absorption and electromagnetic interference shielding properties of SiCf/SiCN composites. Ceram. Int. **42**, 19237–19244 (2016)

59. F. Ye, Q. Song, Z. Zhang, W. Li, S. Zhang, X. Yin, Y. Zhou, H. Tao, Y. Liu, L. Cheng, L. Zhang, H. Li, Direct growth of edge-rich graphene with tunable dielectric properties in porous Si_3N_4 ceramic for broadband high-performance microwave absorption. Adv. Funct. Mater. **28**, 1707205 (2018)

60. Z. Hou, X. Yin, H. Xu, H. Wei, M. Li, L. Cheng, L. Zhang, Reduced graphene oxide/silicon nitride composite for cooperative electromagnetic absorption in wide temperature spectrum with excellent thermal stability. ACS Appl. Mater. Interfaces **11**, 5364–5372 (2019)

61. J. Kuang, T. Xiao, X. Hou, Q. Zheng, Q. Wang, P. Jiang, W. Cao, Microwave synthesis of worm-like SiC nanowires for thin electromagnetic wave absorbing materials. Ceram. Int. **45**, 11660–11667 (2019)